A Reconfigurable Bidirectional Wireless Power Transceiver for Battery-to-Battery Wireless Charging

Mo Huang, *Member, IEEE*, Yan Lu, *Senior Member, IEEE*, and Rui P. Martins, *Fellow, IEEE*

***Abstract*—Battery-to-battery (B2B) wireless charging can take place in many scenarios, such as using a mobile phone to charge another mobile phone, wearable devices, or low-power sensor nodes. To facilitate this wireless power transfer (WPT) function with the minimum additional cost, we propose a monolithic reconfigurable bidirectional WPT transceiver designed for the first time in CMOS, which can be reconfigured between a differential class-D power amplifier (PA) and a full-wave rectifier. Meanwhile, we employed a maximum current charging mode to maximize the B2B charging efficiency, by directly charging the loading battery with the rectifier, and by powering the PA with the sourcing battery. Then, we reduced the number of cascaded WPT stages from five in the conventional design to three. This bidirectional WPT transceiver fabricated in 0.35 μm CMOS occupies 3.9 mm^2 of silicon area. The bidirectional WPT function, verified at 6.78 MHz with only one off-chip capacitor, exhibits peak efficiencies of 91.5% and 58.6% for the receiver and the overall system, respectively, when the output power is 1.55 W.**

***Index Terms*—Battery charger, bidirectional wireless charging, class-d power amplifier (PA), maximum current charging mode (MCCM), receiver, rectifier, transmitter, transceiver, voltage doubler, wireless power transfer (WPT).**

I. Introduction

WIRELESS power transfer (WPT) has been utilized in a wide range of applications, including mobile, wearable, implantable devices, and wireless sensor networks. In consumer electronics, many advanced models of portable and wearable devices have already been integrated with the wireless charging function. Meanwhile, the aftermarket wireless charging accessories are also quite mature now. With WPT technology, people may charge their mobile devices without any effort in public places, e.g., coffee shops and restaurants. Also, WPT technology has a large potential to help the devices to be thinner and

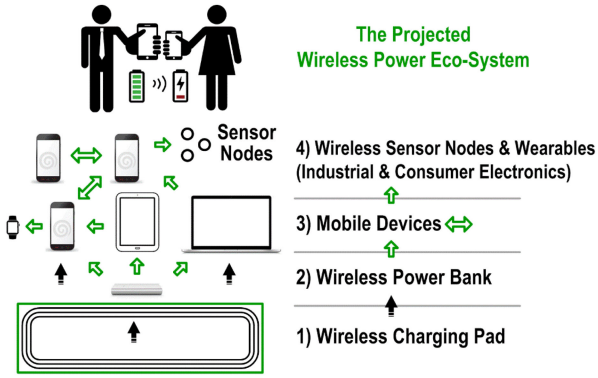

Manuscript received October 7, 2018; accepted November 8, 2018. Date of publication November 14, 2018; date of current version May 22, 2019. This work was supported in part by the Research Committee of University of Macau under Grant MYRG2018-00102-AMSV, in part by Macao Science & Technology Development Fund (FDCT) SKL Fund, and in part by the National Natural Science Foundation of China under Grant 61604044. Recommended for publication by Associate Editor C. K. Tse. *(Corresponding author: Yan Lu.)*

M. Huang was with the State Key Laboratory of Analog and Mixed-Signal VLSI, University of Macau, Macao, China. He is now with the School of Electronics and Information Engineering, South China University of Technology, Guangzhou 510640, China (e-mail:

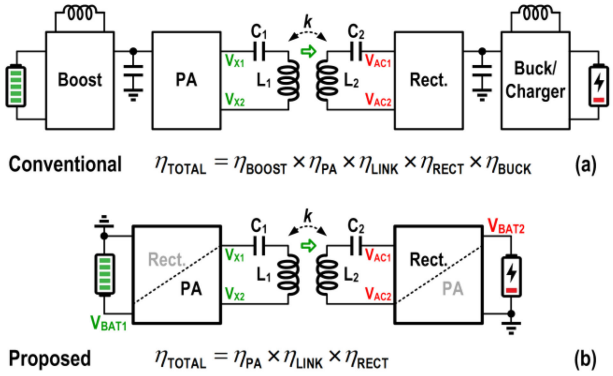

Fig. 2. (a) Bidirectional wireless charging scheme with five cascade stages. (b) MCCM charging scheme with only three stages.

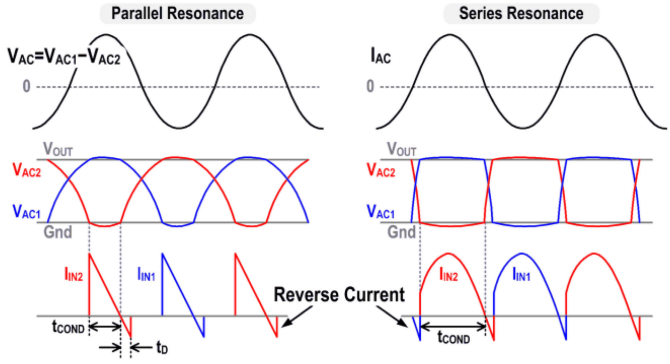

Fig. 3. Comparison on the reverse current sensitivity between parallel and series secondary tanks.

multiple-device charging. The second layer is an intermediate layer formed by wireless power banks which gets energy from the plant feeding the power-hungry mobile devices. The third layer incorporates mobile devices with computation and analysis capabilities, including notebooks, tablets, and mobile phones. The fourth layer contains low power wearables and wireless sensor nodes, which sense and collect the data from the human body or the ambient environment. To facilitate these applications, this work investigates for the first time an on-chip solution for bidirectional wireless charging.

In the conventional pad-to-device wireless charging structure, the wireless power RX consists of a rectifier and a buck-type dc–dc converter for constant-current (CC) and constant-voltage charging mode control [5]. For turning such wireless power RX into a TX for the B2B charging, the buck converter will reverse its operation direction and become a boost converter on the TX side, as shown in Fig. 2(a). In this scenario, we obtain the total B2B charging efficiency (η_{TOTAL}) by multiplying the efficiencies of the five cascaded stages:

$$\eta_{\mathrm{TOTAL}} = \eta_{\mathrm{BOOST}} \times \eta_{\mathrm{PA}} \times \eta_{\mathrm{LINK}} \times \eta_{\mathrm{RECT}} \times \eta_{\mathrm{BUCK}} \quad (1)$$

where $\eta_{\mathrm{BOOST}}, \eta_{\mathrm{PA}}, \eta_{\mathrm{LINK}}, \eta_{\mathrm{RECT}}, \eta_{\mathrm{BUCK}}$ represent the efficiencies of the boost converter, power amplifier (PA), coupling link, rectifier, and buck-type charger, respectively. Apparently, every cascaded stage degrades the total charging efficiency. Meanwhile, the bulky inductor in the dc–dc converter increases the area and cost of the wireless charging module. More importantly, the B2B charging is energy-limited, then, one of our targets is to transfer the energy from one battery to another with the minimum loss and a safe charging current.

To reduce the number of cascaded stages and consequently to increase the B2B charging total efficiency, we employed in this paper a reconfigurable bidirectional wireless power transceiver (TRX) with the maximum current charging mode (MCCM) [6], as shown in Fig. 2(b). With the PA supplied directly by the source battery, the rectifier would charge the loading battery with the maximum available current. Therefore, there are only three essential stages in this system, and the total efficiency is as follows:

$$\eta_{\mathrm{TOTAL}} = \eta_{\mathrm{PA}} \times \eta_{\mathrm{LINK}} \times \eta_{\mathrm{RECT}}. \quad (2)$$

However, without the post-stage regulator, it would be worth investigating whether the output current of the MCCM operation is suitable for battery charging, which is also included in this paper.

We organized this paper as follows. Section II discusses the design considerations of the reconfigurable WPT transceiver topology. Section III analyzes the charging current of the MCCM. Section IV presents the circuit implementations. Section V reveals the measurement results of the proposed WPT transceiver. Finally, Section VI draws the conclusions.

II. Topology of the Bidirectional WPT Transceiver

A. Resonant Tank

For the mobile devices, the area of the wireless charging module is quite limited, and there will be no room to accommodate separate TX and RX resonant coils. Therefore, the resonant tank in the bidirectional TRX should be reused for both TX and RX modes.

Basically, there are two types of resonant tanks: series and parallel. They have quite different characteristics in terms of impedance transformation, voltage and current waveforms. The series resonant tanks will transfer a small load impedance on the secondary side into a relatively large equivalent impedance on the primary side [7], [8], therefore, achieving higher total efficiency in median/high power scenarios, e.g., in our B2B wireless charging case. Meanwhile, the series resonant *LC* tank behaves like an ac current source, while the parallel acts like a voltage source. This feature imposes that the secondary input current magnitude will be nearly independent of its output power [8]. Moreover, the resonant frequency of the secondary series *LC* tank is, regardless of the load, only related to the values of the inductor and the capacitor [7].

From the circuit design perspective, the series resonant is less sensitive to the active diode reverse current as pointed out in [8]. However, we have a different interpretation, for example, let us consider a full-wave rectifier, where V_{AC1} and V_{AC2} are the two rectifier input voltages, and I_{IN1} and I_{IN2} are the differential input currents. As shown in Fig. 3, the parallel resonant tank has sinusoidal-like input voltage waveforms, but with a pulsing input current going into the rectifier. This implies that the rectifier output only draws current during the voltage peaks with short conduction time (t_{COND}). On the other hand, most of the ac current of the resonant tank will go through the rectifier charging up the output, which results in a much longer conduction time. As we know, the turned-off delay time (t_{D}) of the comparator in the active diode determines the duration of the reverse current. Considering an equal t_{D} for both series- and parallel-resonant cases, t_{D} would be a small portion of t_{COND} in

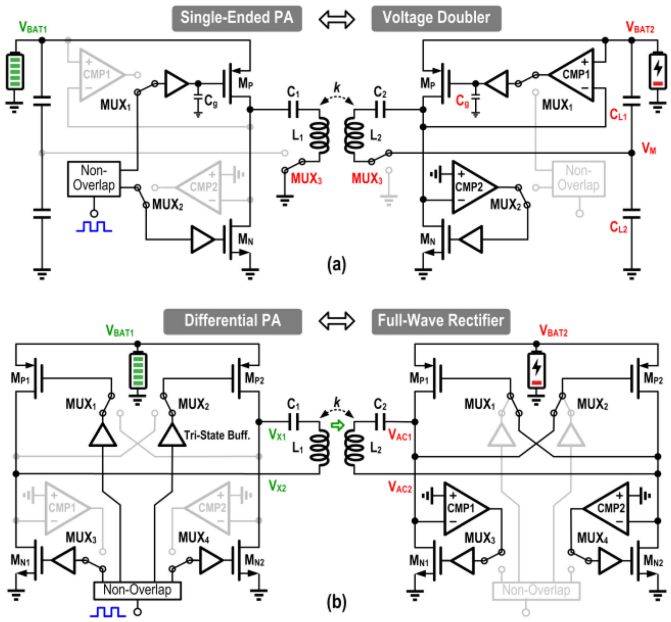

Fig. 4. (a) Topology-1: Bidirectional TRX reconfiguring between single-ended PA and voltage doubler. (b) Topology-2: Reconfiguring between differential PA and full-wave rectifier.

the series resonant case, which indicates a higher efficiency for the series resonant case. Furthermore, the reverse current issue can also be mitigated by applying a series inductor as a compensator for the parallel resonator [9]. Nevertheless, this inductor will increase both the cost and area of the charging module, which may not be favorable for portable/wearable devices.

In sum, in this design, we applied the series resonant tank.

B. Reconfigurable PA and Rectifier

To save cost for the bidirectional charging function, the rectifier should be reconfigured to a PA with negligible area overhead. Basically, there are two possible reconfigurable topologies as presented next.

Topology-1: Fig. 4(a) shows a reconfigurable TRX that can be reconfigured between a single-ended PA and an active voltage doubler by reusing the power transistors ($M_{\mathrm{P,N}}$) and the resonant tank ($C_{1,2}$ and $L_{1,2}$). The reconfiguration uses three multiplexers (MUX_{1-3}). In the TX mode, the non-overlapping signals through MUX_1 and MUX_2 control M_{N} and M_{P}, and MUX_3 connects one terminal of the *LC* tank to the ground. In the RX mode, MUX_1 and MUX_2 enable the comparators for operating M_{N} and M_{P} as active diodes, with one terminal of the *LC* tank shorted to V_{M}. In this way, both the power devices and the resonant tank are reused. Therefore, MUX_1 and MUX_2 are small because they only deal with control signals. On the other hand, MUX_3 should be very large, because it is on the power path and it needs to conduct a large current. In the TX mode, MUX_3 needs to be an NMOS which should have the same size as M_{N}, while in the RX mode, MUX_3 needs to conduct a large current between the *LC* tank and V_{M}. Because V_{M} is a voltage around $\frac{1}{2}V_{\mathrm{BAT2}}$, there should be both NMOS and PMOS switches for MUX_3, which require a silicon area larger than M_{P}. Hence, Topology-1 will at least double the silicon area for the reconfigurable bidirectional structure.

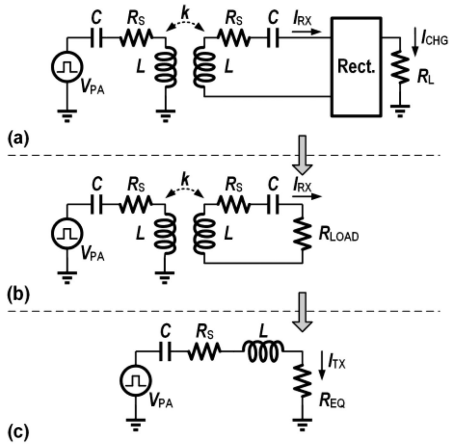

Fig. 5. (a) Simplified model of the WPT system, converted to (b) using R_{LOAD} to model the rectifier input impedance, and to (c) using R_{EQ} to model the TX side equivalent load impedance.

Besides, this reconfigurable TRX Topology-1 has several drawbacks as discussed next. First, MUX_3 not only requires a large area as mentioned above, but also generates additional conduction losses when compared with the conventional unidirectional design. Second, the single-ended PA only has a output peak-to-peak amplitude equal to the battery voltage, which will result in a low output power. Third, the voltage doubler requires two additional load capacitors C_{L1} and C_{L2} connected in series, which will also increase the area and cost [10]. Lastly, the gate of the M_{P} in the voltage doubler needs to be driven by the buffer. On the other hand, for a PMOS cross-connected full-wave rectifier, the ac inputs drive the PMOS power transistors which would significantly reduce the switching loss by recycling the gate-drive energy back to the *LC* resonant tank [11].

Topology-2: The bidirectional TRX can be reconfigured between a differential class-D PA and a full-wave active rectifier, as exhibited in Fig. 4(b). We utilized four power devices ($M_{\mathrm{N1,2}}$ and $M_{\mathrm{P1,2}}$), and four multiplexers (MUX_{1-4}), which are necessary to facilitate the reconfiguration. In the TX mode, MUX_{1-4} connect all the gates of power devices to the non-overlapping gate drivers. In the RX mode, $M_{\mathrm{P1-2}}$ are cross connected, while CMP_{1-2} outputs control $M_{\mathrm{N1-2}}$ as active diodes. In this topology, MUX_{1-4} only deals with gate control signals, and thus can be small-sized with negligible area overhead. And the efficiency of Topology-2 will be higher, because both conduction loss and switching loss are smaller when compared with Topology-1.

C. Charging Current Analysis

Another benefit of Topology-2 is that it achieves almost four times larger charging current I_{CHG} when compared with Topology-1. Fig. 5(a) displays the simplified model of the WPT system. Here, we replace the PA by an ideal ac voltage source with an amplitude of V_{PA}. *L*, *C*, R_{S}, and *k* are the coupling inductor, series capacitor, lumped equivalent series resistor, and coupling coefficient of the inductive coupling link. R_{L} is the equivalent load impedance. And, I_{RX} is the root-mean-square resonant current in the receiving coil. The rectifier block is a voltage doubler for Topology-1 whilst a full-wave rectifier for Topology-2. The relationship between I_{CHG} and I_{RX} can be

presented by the following:

$$\begin{cases} I_{\mathrm{CHG1}} = \frac{1}{\pi} I_{RX1} \\ I_{\mathrm{CHG2}} = \frac{2}{\pi} I_{RX2} \end{cases} \tag{3}$$

with the subscripts 1 and 2 associated to Topology-1 and -2, respectively. Then, as Fig. 5(b) reveals, R_{LOAD} is used to model the rectifier input impedance, which can be calculated as follows [7]:

$$\begin{cases} R_{\mathrm{LOAD1}} = \frac{2 \cdot R_{\mathrm{L}}}{\pi^2 \eta_{\mathrm{RX1}}} \\ R_{\mathrm{LOAD2}} = \frac{8 \cdot R_{\mathrm{L}}}{\pi^2 \eta_{\mathrm{RX2}}} \end{cases} \tag{4}$$

where $2/\pi^2$ and $8/\pi^2$ terms indicate the sinusoidal currents converted to dc after rectification, and η_{RX} represents the rectifier efficiency. Assuming $\eta_{\mathrm{RX1}} = \eta_{\mathrm{RX2}}$, then $R_{\mathrm{LOAD1}} = R_{\mathrm{LOAD2}}/4$.

After that, all the circuits operating around the resonant frequency on the RX side have been transformed into an equivalent impedance R_{EQ} on the TX side, as in Fig. 5(c)

$$R_{\mathrm{EQ}} = k^2 \frac{L}{C} \frac{1}{R_S + R_{\mathrm{LOAD}}}. \tag{5}$$

Considering that R_{S} should be much smaller than R_{LOAD} for a high efficiency design, $R_{\mathrm{EQ1}} \approx 4R_{\mathrm{EQ2}}$, and $I_{\mathrm{TX}} = V_{\mathrm{PA}}/(R_{\mathrm{S}} + R_{\mathrm{EQ}})$, with $I_{\mathrm{TX1}} \approx I_{\mathrm{TX2}}/8$ because $V_{\mathrm{PA2}} = 2V_{\mathrm{PA1}}$ for the differential implementation in Topology-2. I_{RX} can then be derived as follows:

$$I_{\mathrm{TX}}^2 R_{\mathrm{EQ}} = I_{\mathrm{RX}}^2 \left(R_S + R_{\mathrm{LOAD}}\right)$$

$$I_{\mathrm{RX}} = I_{\mathrm{TX}} \sqrt{\frac{R_{\mathrm{EQ}}}{R_S + R_{\mathrm{LOAD}}}} \tag{6}$$

and therefore, we calculate $I_{\mathrm{RX1}} \approx I_{\mathrm{RX2}}/2$. Together with (3), we can obtain $I_{\mathrm{CHG1}} \approx I_{\mathrm{CHG2}}/4$.

To sum up, Topology-2 not only achieves higher efficiency, smaller silicon area and lower cost, but also provides a 4× larger charging current. Therefore, we applied it to the proposed bidirectional wireless power TRX.

III. Maximum Charging Current Mode

To reduce the number of cascaded stages for higher overall B2B wireless charging efficiency, we use the MCCM direct charging scheme. In this prototype, we did not implement any regulation scheme for output voltage or current regulation. This should be reasonable because we found that the output current of the B2B charging system decreases with time, while its maximum value can be lower than the rated maximum charging current (typically battery-capacity/hour) allowed by most of the mobile devices. Therefore, it is natural to directly charge the loading battery with the maximum available current in the B2B case.

Meanwhile, in case the battery capacity is relatively small, e.g., for the wearable devices, the MCCM scheme will also be compatible with the single-stage regulating rectifier schemes proposed in the literature [12]–[19]. For example, a resonant regulating rectifier (3R) using PWM has been proposed in [12] with several additional off-chip components. Reconfigurable resonant regulating rectifiers that configure themselves by operating in multiple modes (1×/2× mode in [13] and 0×/½×/1× mode in [14]) were designed without additional off-chip components. On the other hand, *Q*-modulation with low-frequency operation and multi-cycle *Q*-modulation for low power applications using adaptive switching control were proposed in [15]–[19]. Furthermore, transmitter side output regulation schemes [19], [20], are also available in the implementation of a wireless data feedback loop. Therefore, similar output regulation schemes can also be realized to regulate output voltage and/or current.

The charging current of this B2B wireless charging scheme can be analyzed as follows. First, we apply the first-order approximation to the charging current I_{CHG} with respect to the charging time t as follows:

$$I_{\mathrm{CHG}} = at + b \tag{7}$$

where a is the increasing/decaying factor of I_{CHG} and b is the initial charging current at $t = 0$. Within a short period of the start-charging time t_1, the at_1 term is still much smaller than b, and thus we assume $I_{\mathrm{CHG}} \approx b$ at the beginning of the charging process. Then, at t_1, the loading battery voltage V_{BAT2} is the integral of I_{CHG}, which can be written as follows:

$$V_{\mathrm{BAT2}}(t_1) = \frac{1}{C_{\mathrm{BAT}}} \int_0^{t_1} I_{\mathrm{CHG}} dt = \frac{1}{C_{\mathrm{BAT}}} bt_1 + V_0 \tag{8}$$

where V_0 is the initial battery voltage, and C_{BAT} is the equivalent capacitance of the loading battery. We neglect the output filtering capacitor C_{OUT} (1 μF) here, since $C_{\mathrm{BAT}} >> C_{\mathrm{OUT}}$. Then, the equivalent load impedance Z_{BAT} can be calculated as V_{BAT2}/b with an almost-constant $I_{\mathrm{CHG}} \approx b$ at the beginning:

$$Z_{\mathrm{BAT}}(t_1) = \frac{1}{C_{\mathrm{BAT}}} t_1 + \frac{V_0}{b}. \tag{9}$$

With Z_{BAT} as a function of the charging time t. Then, we calculate I_{CHG} using the method derived in Section II-C, by finding out the corresponding Z_{LOAD} and Z_{EQ}

$$Z_{\mathrm{LOAD}}(t_1) = \frac{8}{\pi^2} \cdot \frac{Z_{\mathrm{BAT}}}{\eta_{\mathrm{RECT}}} \tag{10}$$

for a full-wave rectifier. And Z_{EQ} can be calculated using (5) and (9). Then, I_{CHG} will become

$$I_{\mathrm{CHG}} = \frac{2}{\pi} I_{\mathrm{RX}} = \frac{8}{\pi^2} V_{\mathrm{PA}} \frac{1}{R_S + Z_{\mathrm{EQ}}} \sqrt{\frac{Z_{\mathrm{EQ}}}{R_S + Z_{\mathrm{LOAD}}}}. \tag{11}$$

When substituting (5), (9), and (10) into (11), and comparing the result with (7), the charging coefficients a and b can be obtained as follows:

$$a \approx -\frac{8}{\pi^2 \eta_{\mathrm{RECT}} \beta} \frac{I_0 R_S}{\left(R_S^2 + k^2 \frac{L}{C}\right) C_{\mathrm{BAT}}} \tag{12}$$

where $I_0 = \frac{8}{\pi^2} \frac{k\sqrt{\frac{L}{C}}}{R_S^2 + k^2 \frac{L}{C}} V_{\mathrm{PA}}$, and

$$b \approx \frac{I_0}{2} + \sqrt{\frac{I_0^2}{4} - \frac{8}{\pi^2 \eta_{\mathrm{RECT}} \beta} \cdot \frac{I_0 R_S V_0}{R_S^2 + k^2 \frac{L}{C}}} \tag{13}$$

where β is the correction factor to indicate the non-ideal *LC* resonance.

To verify the derivation, we performed a transistor-level simulation. Fig. 6 exhibits the simulated I_{CHG} transient waveform together with the numerical calculation results, including the design parameters used. From there, we can deduct that the calculated and simulated curves match each other well. The discrepancies may come from the switching/conduction loss of the rectifier, the parasitic series resistor of the C_{BAT} and the approximations made in the I_{CHG} derivation. Here, we use a relatively small 0.47 mF capacitor to emulate the battery capacitance, which significantly saves the simulation

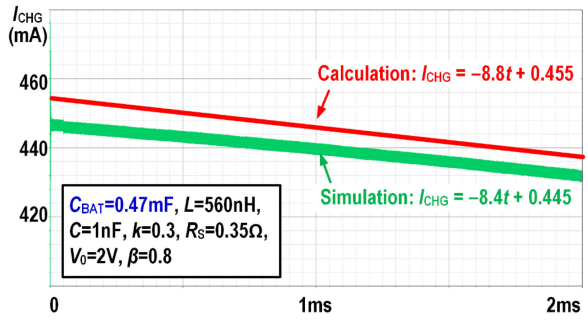

Fig. 6. I_{CHG} versus charging time using numerical calculation and transistor level simulation.

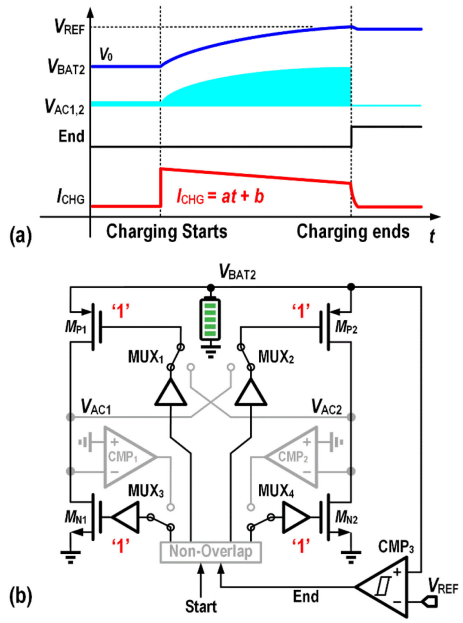

Fig. 7. (a) Transient waveforms of V_{BAT2}, $V_{\mathrm{AC1,2}}$ and I_{CHG} with the proposed charging scheme. (b) Simplified schematic of configuring the bidirectional WPT TRX into the bypass mode.

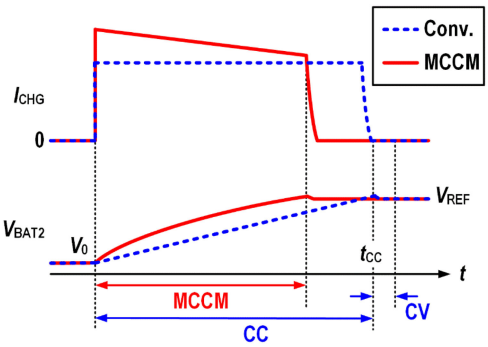

Fig. 8. Comparison between the conventional and the MCCM charging schemes.

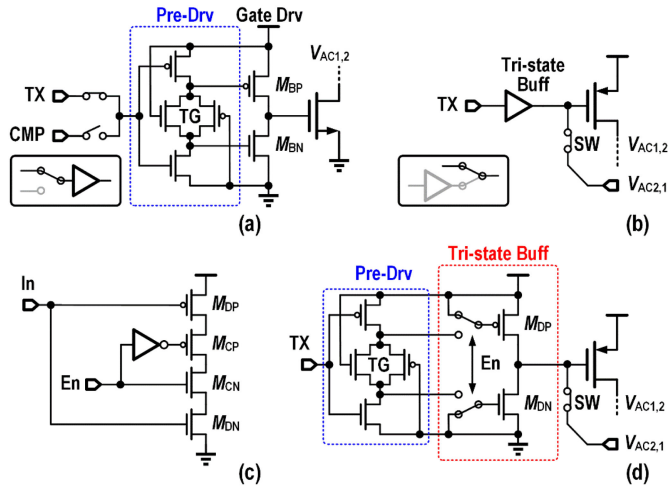

Fig. 9. Schematic of (a) the low-side switch and gate driver, (b) the proposed high-side switch and gate-drive architecture, (c) the conventional tri-state inverter buffer, and (d) the proposed tri-state driver.

time and memory. From (12), we observe that the coefficient a is negative, indicating that the charging current is favorably decaying with time using the MCCM scheme.

Besides, Fig. 7(a) shows the charging control scheme applied to ensure that the charging voltage V_{BAT2} does not exceed the maximum battery voltage V_{REF} for a safe charging. As derived above, I_{CHG} reaches its maximum value b, when the charging process begins. Then, I_{CHG} decreases almost linearly with charging time at a rate of a. When V_{BAT2} exceeds V_{REF}, a hysteresis comparator generates an *End* signal to terminate the charging. Fig. 7(b) displays the schematic for configuring the bidirectional WPT TRX into the bypass mode, which shorts V_{AC1} and V_{AC2} to ground and thus disables the rectifier, imposing I_{CHG} to drop to 0. In addition, the TX should be deactivated as well, by possible wireless data communication methods such as backscattering, near-field communication, or Bluetooth depending on different charging protocols.

Fig. 8 plots the comparison between the conventional and MCCM charging schemes. Obviously, the charging speed would be higher with the MCCM. Because the charging current in the CC mode would be set by the current at the end-point t_{CC} of the CC mode, which would be lower than the maximum available current. Also, since I_{CHG} in MCCM decreases with time, V_{BAT2} can be easily monitored. Again, existing single-stage regulating rectifier schemes are compatible with our reconfigurable bidirectional wireless charging, for output voltage and/or current regulation when necessary.

IV. Circuit Implementation

A. Multiplexer and Gate Driver

As discussed in Section II, to facilitate the bidirectional B2B wireless charging function, multiplexers are necessary to reconfigure the TRX into either a TX or a RX. Fig. 9 presents the MUXs and gate drivers for the low-side NMOS switches and for the high-side PMOS switches. To minimize the size of the MUX, we placed it for the low-side switch before the gate drive buffer (consists of $M_{\mathrm{BN,BP}}$). We also added a transmission gate (TG) to the second last buffer stage to reduce the short-circuit current of the last stage buffer, by turning off the $\mathrm{M_{BN}}$ first before turning on the M_{BP}, and vice versa.

On the other hand, if we place the buffer for the high-side PMOS after the MUX as in Fig. 10(a), gate charging loss will take place. This loss is equal to $C_{\mathrm{g}}V^2 f_{\mathrm{res}}$, where C_{g} is the gate capacitance, and f_{res} is the resonant frequency. Considering a relatively large power transistor size for reduced conduction

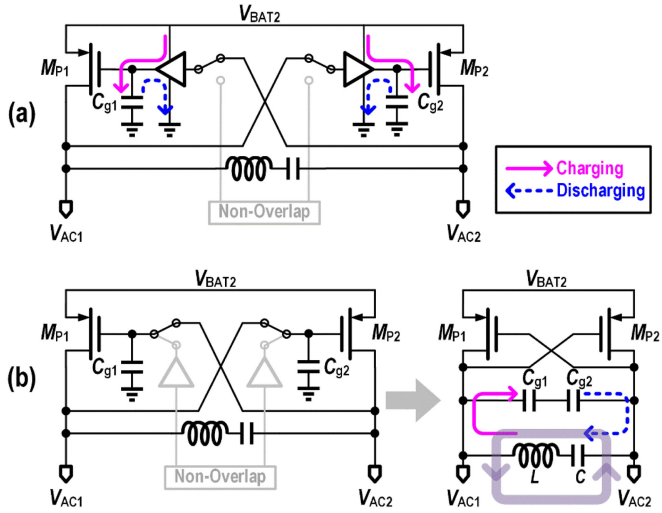

Fig. 10. In the RX mode, (a) M_{P1} and M_{P2} driven by gate drivers with significant gate switching loss and (b) M_{P1} and M_{P2} directly driven by V_{AC1} and V_{AC2}, with the gate capacitors charged/discharged by the resonant circuit.

loss, C_g will cause a significant gate charging loss. To get rid of this, we used a tri-state inverter for the buffer of the high-side switch [see Fig. 9(b)]. In the TX mode, we enable the tri-state inverter for driving the power PMOS. In the RX mode, the tri-state inverter will output high impedance, and the power PMOS will be driven by the ac input. As the input waveforms V_{AC1} and V_{AC2} are differential, the gate capacitors C_{g1} and C_{g2} are equivalent to be series connected as seen by the ac input source, in parallel to the resonant tank. In this scenario, the resonant circuit charges/discharges the gate capacitors as illustrated in Fig. 10(b), being part of the *LC* resonant tank. With this self-driving configuration, the transistor-level simulation shows a roughly 2% improvement on the RX efficiency.

Fig. 9(c) displays a conventional tri-state inverter, where we used control transistors M_{CP} and M_{CN} to provide a high output impedance. All four transistors in the conventional tri-state inverter should be double sized for the same driving capability when compared with a basic inverter. Fig. 9(d) exhibits the tri-state buffer in this paper. We removed M_{CP} and M_{CN}, and inserted two MUXs to control M_{DP} and M_{DN}. The RX mode requires a high output impedance, with the gates of M_{DP} and M_{DN} connected to V_{DD} and ground through the MUXs, respectively. In the TX mode, with M_{DP} and M_{DN} connected to the pre-driver, the short-circuit current can still be prevented.

B. Active Diode

Fig. 11 shows the schematic of the NMOS active diode, based on the common-gate input push–pull comparator that compares V_{AC1} and ground voltage to turn on or off the power transistor M_{N1}. M_{1-4} are the common-gate input pairs. To reduce the reverse current caused by the comparator and buffer delay, we implemented a reverse current control (RCC) scheme with M_{7-8}, by adding additional bias currents to generate an input offset [11]. Then, M_{N1} turns off earlier to compensate for the delay. To prevent the power NMOS being turned-on more than once per cycle, a.k.a. multiple-pulsing problem, the R-S latch will keep the RCC control signal staying low even when V_{GN1} goes up, which means the comparator input offset exists until V_{GN2} goes up. Furthermore, we employed a one-shot logic

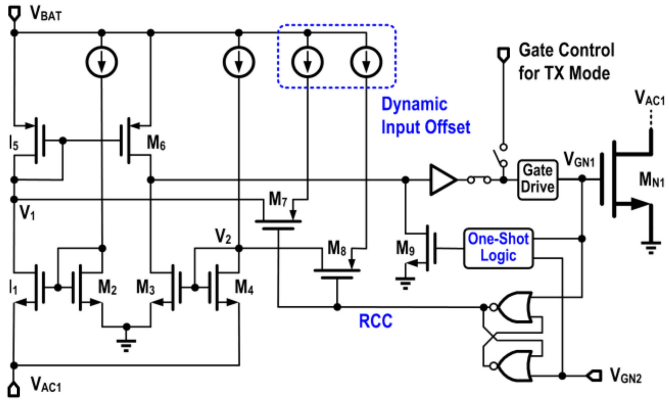

Fig. 11. Schematic of the active diode.

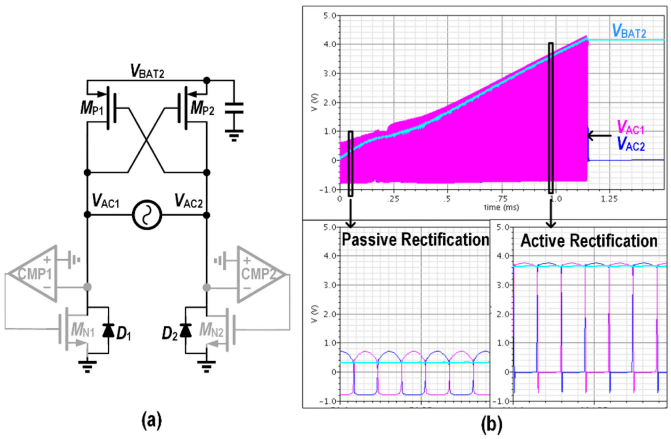

Fig. 12. (a) Active components in the rectifier when V_{BAT2} is low and (b) simulated start-up waveforms of the rectifier, with zoomed-in waveforms of the passive and active rectifications.

detecting the falling-edge of V_{GN1} to pull down the comparator output by M_9, and the logic will be reset when V_{GN2} goes up [8]. Therefore, a hard-off for the comparator can be guaranteed. We also added an MUX before the gate driver to configure it into the RX or TX mode, corresponding to Fig. 9(a).

It should be noted that the comparators and thus the active diodes will be relaxed when V_{BAT2} is low, e.g., during start-up. Instead, the parasitic diodes of the NMOS power transistors [D_1 and D_2 shown in Fig. 12(a)] will work in this scenario. When the input amplitude manages to forward bias one branch on (M_{P1} and D_2, or M_{P2} and D_1) while keeping the other branch off, "passive rectification" will execute and V_{BAT2} will be charged up. Once V_{BAT2} exceeds the threshold to supply the comparators, the "active rectification" with the active diodes will then be enabled. Fig. 12(b) displays the simulated start-up waveforms starting from $V_{BAT2} = 0$.

V. Measurement Results

The proposed reconfigurable WPT TRX with MCCM was fabricated in a 0.35 μm CMOS process with thick metal-4 option. 5 V power devices have been employed to handle the battery voltage level, and to resist high voltage spikes during switching. Fig. 13 shows the chip micrograph of the reconfigurable TRX. The chip area is 3.9 mm^2, mainly occupied by the four power transistors.

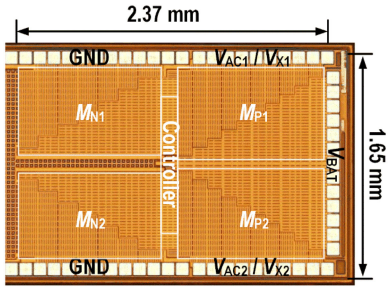

Fig. 13. Chip micrograph of the reconfigurable TRX.

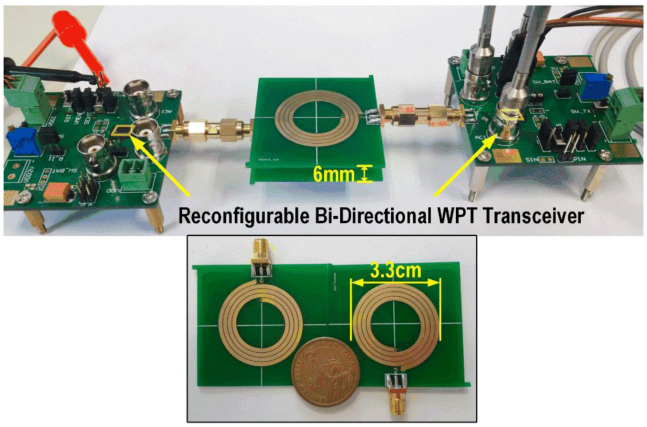

Fig. 14. Measurement setup with two reconfigurable circuit boards and two identical PCB coils.

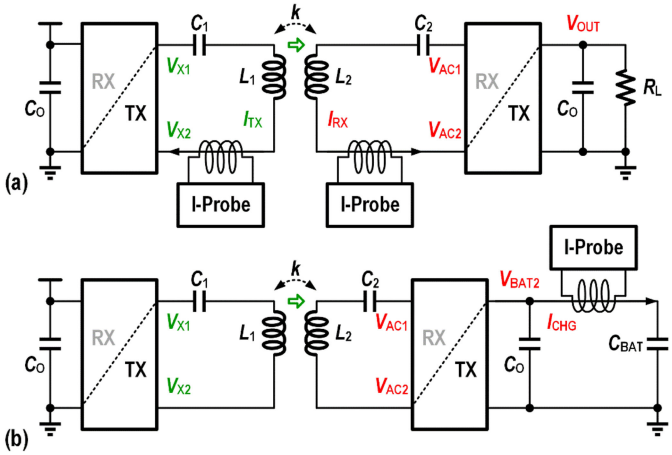

Fig. 15. Test benches with (a) a resistive load and (b) a capacitive load.

Fig. 14 exhibits the measurement setup for the proposed WPT TRX. The identical TX and RX coils are etched on a single-side printed circuit boards (PCBs). Each coil has four turns, with inner and output radii of 1.9 and 3.3 cm, respectively. These two coils were separated by 6 mm during the WPT measurements. The measured inductance L of the coils is 560 nH, and the series resistance R_S is 350 mΩ. And the coupling coefficient k is 0.3. To resonate at 6.78 MHz, we chose a 1 nF capacitor for both the RX and TX. We also utilized two identical transceiver boards in the measurement. They can be reconfigured to either WPT TX or RX by one-single control pin.

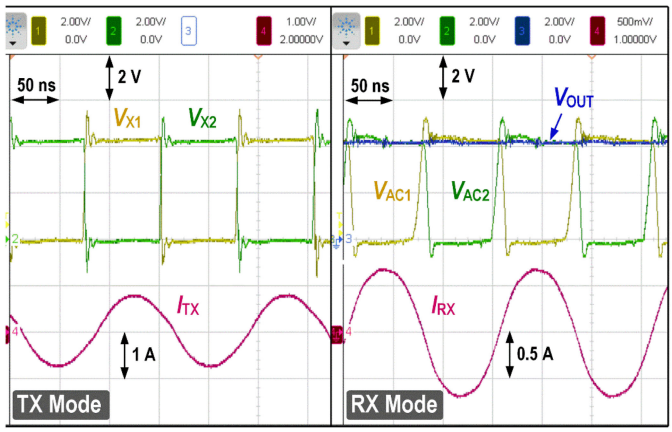

Fig. 16. Measured TX output voltage and current waveforms; ac input voltage and current, and dc output voltage of the RX.

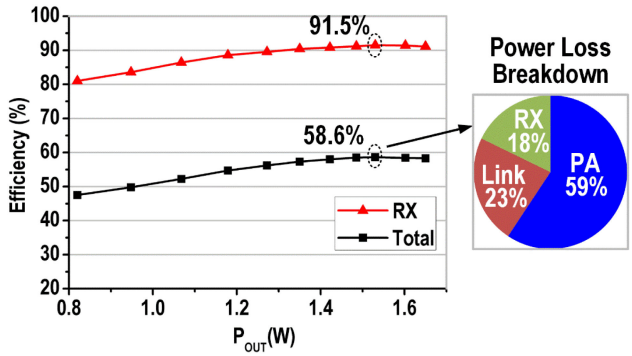

Fig. 17. Measured receiver and total efficiencies versus output power, and power loss breakdown at the peak efficiency.

Two sets of measurements have been performed. Fig. 15(a) presents the setup with resistive load for efficiency measurements, while Fig. 15(b) shows the setup for the I–V charging characteristic measurement. Fig. 16 plots the measured TX and RX voltage and current waveforms with a 10 Ω load resistor. With a 4.2 V dc supply for the TX, we observed square voltage waveforms at the class-D PA outputs, and the ac output current amplitude is about 0.8 A. On the RX side, we detected an ac input current amplitude of 0.7 A and a dc output voltage of 4.1 V.

Fig. 17 shows the RX and total efficiencies of the proposed WPT TRX versus the output power P_{OUT}. The measured peak RX and total efficiencies reach 91.5% and 58.6%, respectively, at 1.55 W P_{OUT}. Fig. 17 also presents the power loss breakdown at the peak-efficiency point. The power losses from the RX, link, and PA are 18%, 23%, and 59%, respectively. This result also indicates that the total efficiency may be further enhanced by improving the PA efficiency, which might be achieved by a better switching dead-time control.

Fig. 18 shows the measured transient waveforms of the RX ac input voltage $V_{\mathrm{AC1,2}}$, charging current I_{CHG}, and the loading battery voltage V_{BAT2}. In this measurement, a 1 mF load capacitor has been used to emulate the battery. The charging process starts at about 1 V of V_{BAT2}, and ends with V_{BAT2} charged to V_{REF} (4.2 V), which takes around 11 ms. During this period, the maximum/initial charging current is $b = 390$ mA with an attenuation of $a = -5$ A/s, basically matching with the calculated $b = 470$ mA and $a = -3.6$ A/s. The discrepancies should

TABLE I
COMPARISON WITH STATE-OF-THE-ART WORKS

	[12] 2013	[14] 2016	[15] 2015	[21] 2015	[22] 2016	**This work**
Process (μm)	0.35 BCD	0.35 CMOS	0.35 CMOS	0.35 CMOS	0.18 BCD	**0.35 CMOS**
Area (mm^2)	5.52	4.77	4.8	2.42/3*	5.83	**3.9**
WPT Direction	Uni-dir.	Uni-dir.	Uni-dir.	Uni-dir.	Uni-dir.	**Bi-dir.**
RX Topology	3R	R^3	Rect.+LDO	R^3	Rect.+Buck	**Direct Charge**
Max. V_{OUT} (V)	5	5	4.7	3.7	10	**4.2**
$f_{Resonant}$ (MHz)	6.78	6.78	2	13.56	6.78	**6.78**
Max. P_{OUT} (W)	6	6	1.45	0.23	2.5	**1.6**
η_{RX}	86%	92.2%	76%	92.5%	91.2%	**91.5%**
η_{Total}	55%	N/A	N/A	62.4%	54%	**58.6%**
Off-chip Components	5 diodes, 3 caps.	1 cap.	3 caps.	1 cap.	1 cap.	**1 cap.**

*RX and TX area, respectively.

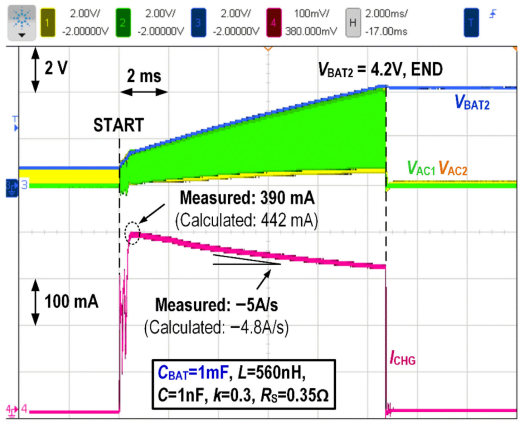

Fig. 18. Measured ac input voltage, charging current, and output voltage when charging a 1 mF capacitor with MCCM.

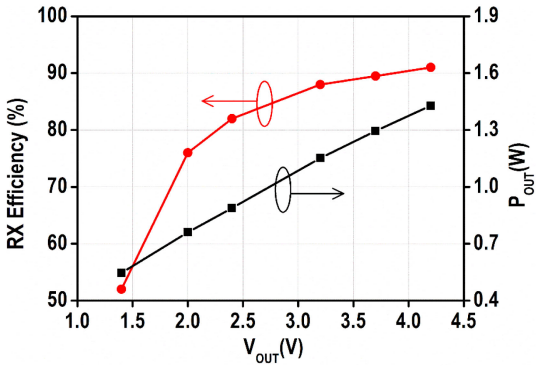

Fig. 19. Measured RX efficiency and P_{OUT} versus V_{OUT} during the charging process, with the same link parameters given in Fig. 18.

come from the additional power loss of the capacitor (battery) parasitic ESR, PCB trace parasitics, and the resonant frequency offset. After V_{BAT2} reaches 4.2 V, the rectifier is deactivated, and then I_{CHG} goes down with V_{BAT2} kept constant. Fig. 19 shows the measured RX efficiency and P_{OUT} versus V_{OUT}.

Table I compares the performances of the proposed reconfigurable WPT TRX with state-of-the-art designs. This paper achieves comparable or sometime even better receiver and total efficiencies, indicating that the reconfigurable function does not degrade other performances. Moreover, the reconfigurable architecture and MCCM also help to reduce the off-chip components and will lower the cost.

VI. CONCLUSION

This paper presented a reconfigurable WPT transceiver for bidirectional B2B wireless charging, with possible applications in both consumer and industrial electronics. After comparing and discussing two TRX solutions, we chose a reconfigurable TRX with a differential class-D PA as the TX and a full-wave rectifier as the RX for smaller area, higher efficiency, and larger charging current. Moreover, to improve the total charging efficiency, we proposed the MCCM scheme to charge the battery directly without any current or voltage regulation. With two identical reconfigurable WPT transceivers and PCB coils, the measurement results verified the bidirectional function with the minimum number of off-chip components, and demonstrated good efficiencies for both the receiver and the overall system.

REFERENCES

[1] "Wireless charging market to reach $37.2 billion, globally by 2022," Allied Market Research. 2018. [Online]. Available: https://www.alliedmarketresearch.com/wireless-charging-market. Accessed on: Apr. 3, 2018.
[2] U. K. Madawala and D. J. Thrimawithana, "A bidirectional inductive power interface for electric vehicles in V2G systems," *IEEE Trans. Ind. Electron.*, vol. 58, no. 10, pp. 4789–4796, Oct. 2011.
[3] J. Lee and B. Han, "A bidirectional wireless power transfer EV charger using self-resonant PWM," *IEEE Trans. Power Electron.*, vol. 30, no. 4, pp. 1784–1787, Apr. 2015.
[4] C. Huang and C. Lin, "Wireless power and bidirectional data transfer scheme for battery charger," *IEEE Trans Power Electron.*, vol. 33, no. 6, pp. 4679–4689, Jun. 2018.
[5] H. Park *et al.*, "A design of a wireless power receiving unit with a high-efficiency 6.78-MHz active rectifier using shared DLLs for magnetic-resonant A4 WP applications," *IEEE Trans. Power Electron.*, vol. 31, no. 6, pp. 4484–4498, Jun. 2016.
[6] M. Huang, Y. Lu, S. P. U, and R. P. Martins, "A reconfigurable bidirectional wireless power transceiver with maximum current charging mode and 58.6% battery-to-battery efficiency," in *Proc. IEEE Int. Solid-State Circuits Conf.*, Feb. 2017, pp. 376–377.
[7] K. Van Schuylenbergh and R. Puers, *Inductive Powering: Basic Theory and Application to Biomedical Systems*. Dordrecht, The Netherlands: Springer, 2009.
[8] L. Cheng, W. H. Ki, Y. Lu, and T. S. Yim, "Adaptive on/off delay-compensated active rectifiers for wireless power transfer systems," *IEEE J. Solid-State Circuits*, vol. 51, no. 3, pp. 712–723, Mar. 2016.
[9] X. Qu, Y. Jing, H. Han, S. Wong, and C. K. Tse, "Higher order compensation for inductive-power-transfer converters with constant-voltage or constant-current output combating transformer parameter constraints," *IEEE Trans Power Electron.*, vol. 32, no. 1, pp. 394–405, Jan. 2017.
[10] Y. Lu, M. Huang, L. Cheng, W. H. Ki, S. P. U, and R. P. Martins, "A dual-output wireless power transfer system with active rectifier and three-level operation," *IEEE Trans. Power Electron.*, vol. 32, no. 2, pp. 927–930, Feb. 2017.

[11] Y. Lu and W.-H. Ki, "A 13.56 MHz CMOS active rectifier with switched-offset and compensated biasing for biomedical wireless power transfer systems," *IEEE Trans. Biomed. Circuits Syst.*, vol. 8, no. 3, pp. 334–344, Jun. 2014.
[12] J.-H. Choi, S.-K. Yeo, S. Park, J.-S. Lee, and G.-H. Cho, "Resonant regulating rectifiers (3R) operating for 6.78 MHz resonant wireless power transfer (RWPT)," *IEEE J. Solid-State Circuits*, vol. 48, no. 12, pp. 2989–3001, Dec. 2013.
[13] X. Li, C.-Y. Tsui, and W.-H. Ki, "A 13.56 MHz wireless power transfer system with reconfigurable resonant regulating rectifier and wireless power control for implantable medical devices," *IEEE J. Solid-State Circuits*, vol. 50, no. 4, pp. 978–989, Apr. 2015.
[14] L. Cheng, W. H. Ki, and C. Y. Tsui, "A 6.78-MHz single-stage wireless power receiver using a 3-mode reconfigurable resonant regulating rectifier," *IEEE J. Solid-State Circuits*, vol. 52, no. 5, pp. 1412–1423, May 2017.
[15] M. Kiani, B. Lee, P. Yeon, and M. Ghovanloo, "A Q-modulation technique for efficient inductive power transmission," *IEEE J. Solid-State Circuits*, vol. 50, no. 12, pp. 2839–2848, Dec. 2015.
[16] B. Lee, P. Yeon, and M. Ghovanloo, "A multicycle Q-modulation for dynamic optimization of inductive links," *IEEE Trans. Ind. Electron.*, vol. 63, no. 8, pp. 5091–5100, Aug. 2016.
[17] M. Choi, T. Jang, J. Jeong, S. Jeong, D. Blaauw, and D. Sylvester, "A resonant current-mode wireless power receiver and battery charger with -32 dBm sensitivity for implantable systems," *IEEE J. Solid-State Circuits*, vol. 51, no. 12, pp. 2880–2892, Dec. 2016.
[18] H. S. Gougheri and M. Kiani, "Current-based resonant power delivery with multi-cycle switching for extended-range inductive power transmission," *IEEE Trans. Circuits Syst. I, Reg. Papers*, vol. 63, no. 9, pp. 1543–1552, Sep. 2016.
[19] D. Ahn, S. Kim, J. Moon, and I. K. Cho, "Wireless power transfer with automatic feedback control of load resistance transformation," *IEEE Trans. Power Electron.*, vol. 31, no. 11, pp. 7876–7886, Nov. 2016.
[20] K. Tomita, R. Shinoda, T. Kuroda, and H. Ishikuro, "1-W 3.3–16.3-V boosting wireless power transfer circuits with vector summing power controller," *IEEE J. Solid-State Circuits*, vol. 47, no. 11, pp. 2576–2585, Nov. 2012.
[21] R. Shinoda, K. Tomita, Y. Hasegawa, and H. Ishikuro, "Voltage-boosting wireless power delivery system with fast load tracker by $\Delta\Sigma$-modulated sub-harmonic resonant switching," in *Proc. IEEE Int. Solid-State Circuits Conf.*, Feb. 2012, pp. 288–290.
[22] X. Li, X. Meng, C. Y. Tsui, and W. H. Ki, "Reconfigurable resonant regulating rectifier with primary equalization for extended coupling- and loading-range in bio-implant wireless power transfer," *IEEE Trans. Biomed. Circuits Syst.*, vol. 9, no. 6, pp. 875–884, Dec. 2015.
[23] J. T. Hwang *et al*., "An all-in-one (Qi, PMA and A4WP) 2.5W fully integrated wireless battery charger IC for wearable applications," in *Proc. IEEE Int. Solid-State Circuits Conf.*, Feb. 2016, pp. 378–380.

Mo Huang (M'15) received the B.Sc., M.Sc., and Ph.D. degrees in microelectronics and solid-state electronics from Sun Yat-sen University, Guangzhou, China, in 2005, 2008, and 2014, respectively.

From 2008 to 2014, he was an IC design Engineer and a Project Manager with Rising Microelectronics, Guangzhou. He was a Research Associate with Nanyang Technological University, Singapore, in 2014. From 2015 to 2016, he was a Postdoctoral Fellow with the State Key Laboratory of Analog and Mixed-Signal VLSI, University of Macau, Macao, China. In October 2016, he joined the School of Electronic and Information Engineering, South China University of Technology, Guangzhou, as an Associate Professor. His current research interests include analog and mixed-signal IC designs, power management IC designs, and wireless power transfer.

Dr. Huang served as a Technical Program Committee Member of IEEE APCCAS 2018, ICTA 2018, ASICON 2017, and Reviewer of many journals/conferences. He was the recipient of IEEE ISSCC 2017 Takuo Sugano Award for Outstanding Far-East Paper, and the IEEE TENCON 2015 Professional Award.

Yan Lu (S'12–M'14–SM'17) received the Ph.D. degree in electronic and computer engineering from the Hong Kong University of Science and Technology, Hong Kong, in 2013.

In 2014, he joined the State Key Laboratory of Analog and Mixed-Signal VLSI of University of Macau as an Assistant Professor. His research interests include, but not limited to, wireless power transfer circuits and systems, low-power analog circuits, and next-generation power management solutions. He has coauthored more than 60 peer-reviewed technical papers, one book entitled *CMOS Integrated Circuit Design for Wireless Power Transfer* (Springer), and edited one book entitled *Selected Topics in Power, RF, and Mixed-Signal ICs* (River Publishers).

Dr. Lu served as a Guest Editor of IEEE TCAS-II in 2018, and served as a Track-Chair/Member of Technical Program Committee of several IEEE conferences (e.g., CICC, ISCAS, and APCCAS). He was the recipient/corecipient of the 2018 Macao Science and Technology Award (2nd prize, with the 1st prize vacancy), the IEEE Solid-State Circuits Society Pre-doctoral Achievement Award 2013–2014, the IEEE CAS Society Outstanding Young Author Award 2017, and the ISSCC 2017 Takuo Sugano Award for Outstanding Far-East Paper.

Rui P. Martins (M'88–SM'99–F'08) was born in April 30, 1957. He received the bachelor's (5-years), master's, and Ph.D. degrees, as well as the Habilitation for Full-Professor in electrical engineering and computers from the Department of Electrical and Computer Engineering, Instituto Superior Técnico (IST), TU of Lisbon, Lisbon, Portugal, in 1980, 1985, 1992, and 2001, respectively.

He has been with the Department of Electrical and Computer Engineering (DECE) / IST, TU of Lisbon, since October 1980. Since 1992, he has been on leave from IST, TU of Lisbon (now University of Lisbon since 2013), and is also with the Department of Electrical and Computer Engineering, Faculty of Science and Technology (FST), University of Macau (UM), Macao, China, where he has been a Chair-Professor since August 2013. In FST, he was the Dean of the Faculty from 1994 to 1997 and he has been the Vice-Rector of the University of Macau since 1997. From September 2008, after the reform of the UM Charter, he was nominated Vice-Rector (Research) until August 31, 2018 and reappointed as Vice-Rector (Global Affairs) until August 31, 2023. Within the scope of his teaching and research activities, he has taught 21 bachelor and master courses and has supervised (or cosupervised) 45 theses, Ph.D. (24) and masters (21). He has coauthored 7 books and 11 book chapters, 30 patents, USA (28) & Taiwan (2), 464 papers, in scientific journals (162) and in conference proceedings (302), as well as other 64 academic works, in a total of 576 publications. He was a Co-Founder of Chipidea Microelectronics (Macao) [now Synopsys] in 2001/2002, and created the Analog and Mixed-Signal VLSI Research Laboratory of UM in 2003, elevated in January 2011 to State Key Laboratory of China (the 1st in Engineering in Macao), being its Founding Director.

Dr. Martins was the Founding Chairman of both IEEE Macau Section (2003–) and IEEE Macau Joint-Chapter on Circuits and Systems (CAS) / Communications (COM) (2005–2008) [2009 World Chapter of the Year of IEEE CAS Society (CASS)]. He was General Chair of 2008 IEEE Asia-Pacific Conference on CAS – APCCAS'2008, and was the Vice-President for Region 10 (Asia, Australia and the Pacific) of IEEE CASS (2009-2011). Since then, he was the Vice-President (World) Regional Activities and Membership of IEEE CASS (2012-2013), and an Associate Editor of IEEE TRANSACTIONS ON CAS II: EXPRESS BRIEFS (2010–2013), also nominated as Best Associate Editor of T-CAS II for 2012 to 2013. He was a member of the IEEE CASS Fellow Evaluation Committee (2013, 2014 and 2019), and CAS Society representative in the Nominating Committee, for the election in 2014, of the Division I (CASS/EDS/SSCS)—Director of the IEEE. He was the General Chair of the ACM/IEEE Asia South Pacific Design Automation Conference – ASP-DAC'2016. He is a Nominations Committee Member of IEEE CASS (2016-2017) and was the Chair of the IEEE CASS Fellow Evaluation Committee (Class 2018). He was the recipient of two government decorations: the Medal of Professional Merit from Macao Government (Portuguese Administration) in 1999, and the Honorary Title of Value from Macao SAR Government (Chinese Administration) in 2001, also the IEEE Council on Electronic Design Automation (CEDA) Outstanding Service Award 2016. In July 2010, he was elected, unanimously, as Corresponding Member of the Portuguese Academy of Sciences (in Lisbon), being the only Portuguese Academician living in Asia.